Mg doping enhanced magnetoelectric effect in the polar magnet $Fe_2Mo_3O_8$

Junkai Yang,[1,2] Dan Su,[1,2] Jincheng He,[1,2] Yu Ji,[1,2] Qinwen Guo,[1,2] Ying Meng,[1,2] Xiangfei Li,[1,2] Luyao Wang,[1,2] Xi Shen,[1,*] Yuan Yao,[1] Youwen Long,[1,2] Young Sun,[4,†] and Richeng Yu[1,2,3,‡]

[1]*Beijing National Laboratory for Condensed Matter Physics, Institute of Physics, Chinese Academy of Sciences, Beijing 100190, People's Republic of China*

[2]*School of Physical Sciences, University of Chinese Academy of Sciences, Beijing 100049, People's Republic of China*

[3]*Songshan Lake Materials Laboratory, Dongguan, Guangdong 523808, People's Republic of China*

[4]*Center of Quantum Materials and Devices and Department of Applied Physics, Chongqing University, Chongqing 401331, People's Republic of China*

(Received 19 September 2022; revised 5 February 2023; accepted 28 February 2023; published 10 March 2023)

Magnetoelectric (ME) effect has given rise to a new design principle for novel low-power electronic devices. The polar magnet $Fe_2Mo_3O_8$ with linear ME effect is one of the promising candidates. Unfortunately, for this material, a large ME response only appears in the ferrimagnetic state, which needs a high magnetic field to be activated. In this work, we successfully synthesize single-crystal $(Fe_{0.95}Mg_{0.05})_2Mo_3O_8$ (FMMO), which achieves a linear ME effect in the antiferromagnetic ground state and shows a significantly improved ME coefficient in the ferrimagnetic state. Compared with the parent phase, six times linear ME coefficient and more than ten orders of magnitude second-order ME coefficient are accomplished in the FMMO. The spin-lattice coupling and the exchange-striction mechanism are believed to play a crucial role in creating the giant ME effect. The present study provides an idea for designing materials with strong ME coupling.

DOI: 10.1103/PhysRevB.107.104408

I. INTRODUCTION

Magnetism and electricity are two fundamental physical phenomena that lead to a broad technological revolution. The crossover between these two fascinating topics, i.e., the magnetoelectric (ME) effect, has attracted much interest recently because of its inestimable scientific significance [1–3] and possible applications [4,5]. Multiferroics are potential materials for obtaining strong ME coupling because of their large electric and magnetic susceptibility [6]. However, after decades of intensive studies, some major bottlenecks still limit the practical applications of multiferroics. For example, the ME response is usually weak in type-I multiferroics, such as $BiFeO_3$ [7], due to the independent origins of ferroelectricity and magnetism. Although type-II multiferroics may possess strong ME coupling, the nonzero electric polarization often appears at low temperatures [8]. As for thin-film composites, it is still hard to achieve reliable control because of the fragile interfacial exchange coupling [9]. Another crucial problem relevant to real technological applications is finding the E-controllable magnetic states since applying electric field is more practical in small devices. In several multiferroics, such as $RMnO_3$ [10], RMn_2O_5 [11], Ca_3CoMnO_6 [12], and $CuFeO_2$ [13], the external magnetic field induces spin reorientation with large polarization change. However, the external electric field influences magnetism weakly in most of these materials. Based on the dilemma of multiferroics discussed above, we need a distinct and more promising strategy to explore new ME materials.

From the Landau phenomenological theory, symmetry conditions play an essential role in ME materials [14]. Accordingly, a route to the colossal ME effect is considering the magnetic systems with polar structures. Such polar crystallographic groups naturally lack space-inversion symmetry and break time-reversal symmetry by forming long-range magnetic order [15], which meets the prerequisite for the nontrivial ME effect. Moreover, some polar magnets like Ni_3TeO_6 [16] and $CaBaCo_4O_7$ [17] are sensitive to a small external stimulus at the phase boundary. In other words, due to the slight energy difference in these materials, the competition among different phases also provides a very productive strategy to control the magnetization by electric fields. A targeted search for the colossal ME effect in polar magnets is meaningful.

Recently, a considerable polarization accompanied by a pronounced ME effect in the family of $M_2Mo_3O_8$ (M = Mn, Fe, Co, Ni) has drawn strong attention [18–21]. The $M_2Mo_3O_8$ belongs to a polar space group $P6_3mc$ [22], allowing the crystallographic polarity along the c axis. The crystal structure can be seen as stacked honeycomblike M_2 layers and kagomelike Mo_3 layers along the c axis [Fig. 1(a)]. In this family, $Fe_2Mo_3O_8$ is more appealing to researchers due to its interesting properties, including the terahertz nonreciprocal directional dichroism [23], a giant thermal Hall effect [24], and the colossal ME effect [19]. According to the first-principles calculations [19,25], the spin-lattice coupling is the dominant mechanism for the thermal Hall effect and the ME effect. However, so far, no direct experimental evidence is available. The lack of measurements of lattice

*xshen@iphy.ac.cn
†youngsun@cqu.edu.cn
‡rcyu@iphy.ac.cn

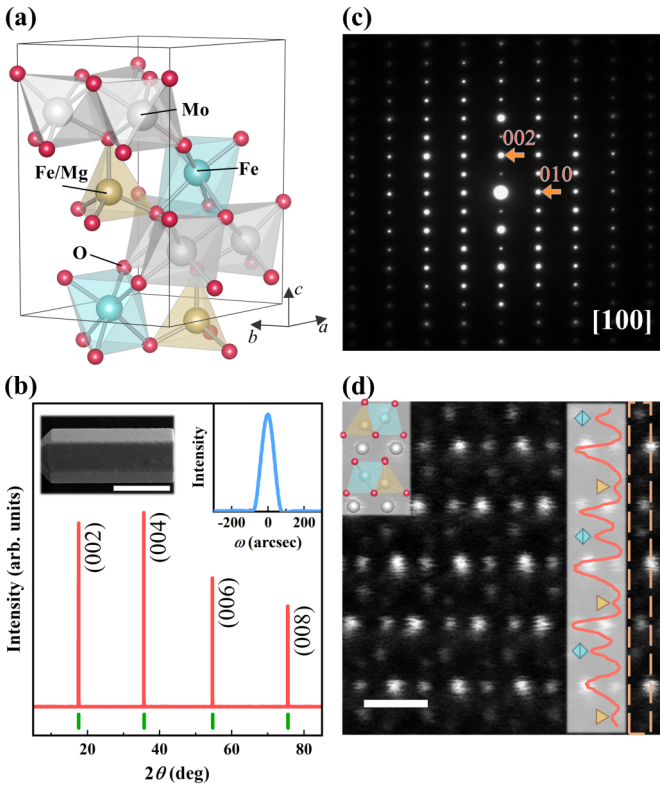

FIG. 1. Structural characterizations of FMMO. (a) Crystalline structure of FMMO. (b) XRD pattern of as-grown single crystal, with insets showing the image and XRD ω-rocking curve of crystal. Scale bar of low-magnification SEM image is 1 mm. (c) SAED pattern of FMMO along the [100] zone axis. (d) Corresponding HAADF image with an overlaid structural model and scale bar being 0.5 nm. White and red spheres represent Mo and O atoms, respectively. Yellow and blue spheres denote Fe/Mg atoms in tetrahedrons and octahedrons, respectively. Red curve is the line profile corresponding to the orange dashed box. Yellow and blue symbols refer to positions of tetrahedral and octahedral oxygen coordinations, respectively.

parameters under magnetic fields prevents further exploration of the ME coupling origin. Moreover, the linear ME effect of $Fe_2Mo_3O_8$ only occurs in the ferrimagnetic (FIM) state, which needs a giant magnetic bias. Partial nonmagnetic ions substitution achieves the tuning of the magnetic exchange interaction and the ME property in many materials [26,27]. This might also be an effective way to solve such an urgent problem in $Fe_2Mo_3O_8$.

Motivated by these facts, we focus on an unexplored member of this family, i.e., $(Fe_{0.95}Mg_{0.05})_2Mo_3O_8$ (FMMO). Considering that the ME effect is one of the core issues addressed in this work and might be elusive in the polycrystal [28,29], we eventually synthesize single-crystal samples after several attempts. In the following, we systematically investigate the structure, magnetism, dielectric property, and magnetostriction of FMMO single crystal. It is confirmed that the Mg^{2+} ions are more likely to substitute the Fe^{2+} ions in tetrahedra. In the H-T phase diagram, it is clear that Mg doping creates two novel metamagnetic states. Remarkably, we observe linear ME coupling in the antiferromagnetic (AFM) state and significantly improved ME coefficient in the FIM state after Mg doping. The present study also unravels that the modulation of magnetostriction accompanies the polarization along the c axis. The significant ME response results in polarization switching with external magnetic fields or magnetization switching with external electric fields. Our results demonstrate the possibility of polar magnets serving as ME devices and indicate that appropriate chemical doping can further enhance their ME coupling.

II. METHODS

$(Fe_{1-x}Mg_x)_2Mo_3O_8 (x = 0,\ 0.05)$ single crystals were grown by the chemical vapor transport reaction [30]. High-purity raw materials (Fe, Fe_2O_3, MoO_2, and MgO) and transporting agent $TeCl_4$ were sealed into evacuated silica tubes and placed into a two-zone furnace at 1000 °C over 10 days for crystals to grow. The crystal structure and quality for each of these single crystals were characterized by an x-ray diffractometer (Rigaku, Ultima IV). The scanning electron microscopy (SEM; Hitachi, Regulus 8230) and transmission electron microscopy (TEM; JEOL, 2100Plus) combined with energy dispersive x-ray (EDX) spectroscopy were used to analyze the chemical compositions. The TEM and scanning TEM (STEM) specimens were prepared by focused ion beam milling (FEI, Helios 600i). The atomic structure was characterized with a transmission electron microscope (JEOL, ARM 200F) equipped with double spherical aberration correctors. The available spatial resolution for each STEM image is better than 78 pm at 200 kV.

The molar susceptibility (χ_m) and field dependence of magnetization (M) were measured by using a magnetic property measurement system (Quantum Design, MPMS-3). The specimen was polished into a typical 1-mm-diameter and 0.12-mm-thick disklike one. Silver paste electrodes were painted on the parallel end surfaces of the specimen to measure the relative dielectric constant (ε_r) and electric polarization (P). These electrical properties were measured by using a physical property measurement system (Quantum Design, PPMS-9T). The values of ε_r were measured at different frequencies by using an *LCR* meter (Agilent, E4980A). The value of P was deduced by time integration of the polarization current measured via a precise electrometer (Keithley, 6517B). The positive direction of P along the c axis is determined by the sign of pyroelectricity in the paramagnetic (PM) phase. For the pyroelectric current (J) measurement, the sample was cooled from 80 to 20 K with a poling electric field ($E_{pol} = \pm 862$ kV m^{-1}). J was recorded after removing E_{pol} and releasing space charges for at least 30 min to exclude possible extrinsic contributions. A high-resolution capacitance dilatometer (Andeen Hagerling, 2700A) was employed to measure the magnetostriction [31] in a cryogen-free superconducting magnet system (Oxford Instruments, TeslatronPT). The temperature- and magnetic-field-dependent ε_r and J were measured at a 2 K min^{-1} warming rate and ramping magnetic field with an increase rate of 100 Oe s^{-1}.

III. RESULTS

A. Crystal structure

The room-temperature slow-scan x-ray diffraction (XRD) pattern focusing on the hexagonal plane of the FMMO crystal

is shown in Fig. 1(b). The four sharp and intense peaks are well indexed to the (00l) reflections of $Fe_2Mo_3O_8$ (ICSD 61069), indicating the high-quality single crystal with the space group $P6_3mc$. As shown in the inset of Fig. 1(b), the XRD rocking curve peak of the (002) plane has a full width at half maximum of 72 arcsec, indicating the highly crystalline nature. A morphology of one typical as-grown crystal of FMMO with large dimensions of 2 mm × 1 mm × 1 mm is also exhibited in Fig. 1(b). The crystal symmetry of FMMO was further confirmed by selected-area electron diffraction (SAED) patterns. Figure 1(c) shows the SAED pattern of FMMO along the [100] zone axis, which is consistent with the result of $Fe_2Mo_3O_8$ [32]. According to the symmetry operations of the $P6_3mc$ space group, the reflections of (00l) should be extinct when l equals an odd number. Even so, these diffraction spots can be seen in Fig. 1(c) due to the multiple scattering of the electron beam along the low-index zone.

The content and distribution of Mg in the crystal are analyzed by SEM-EDX at different crystal positions. The EDX spectrum clearly shows that the sample is composed of Fe, Mg, Mo, and O [Supplemental Material Fig. S1(a) [32]]. Furthermore, Mg with about 5% in content is uniformly distributed in the crystal, which is consistent with the result from TEM-EDX [Fig. S1(b)]. As shown in Fig. 1(a), the Fe layer is formed by two nonequivalent sites in the ab plane, i.e., tetrahedral coordination and octahedral coordination of oxygen. To further explore the crystal structure, we obtain high-angle annular dark-field (HAADF) images of FMMO and $Fe_2Mo_3O_8$ as shown in Fig. 1(d) and Fig. S2(b), respectively. As is well known, the intensity in the HAADF image is sensitive to atomic number Z, making it possible to investigate the positions of Mg^{2+} ions. Compared with $Fe_2Mo_3O_8$, the intensity of the Fe at tetrahedral oxygen coordination is weakened by doping Mg. Because there is no superlattice reflection in the SAED pattern, we conclude that the Mg^{2+} ions occupy the tetrahedral sites randomly. This conclusion is supported by the fact that the ionic radius of Mg^{2+} in coordination number 4 or 6 is slightly smaller than that of Fe^{2+} (high spin) [33]. Previous studies of $Fe_2Mo_3O_8$ suggested that such a preferred occupation for nonmagnetic ions will dilute the magnetic state competition [34]. From this point of view, it is worth further exploring the magnetic property of FMMO.

B. Hidden magnetic states and ME coupling

The temperature dependence of χ_m of FMMO parallel to the c axis is measured at $\mu_0 H = 0.1$ T after zero-field cooling and field cooling, and the results are shown in Fig. 2(a). According to the powder neutron diffraction study of $Fe_2Mo_3O_8$ [35,36], the collinear AFM order is formed along the c axis below 60 K. Similarly, the χ_m of FMMO starts to drop at the onset temperature of the Néel transition ($T_N \approx 60$ K) and approaches to zero at low temperatures. Such a sharp AFM transition reconfirms the preferential occupation of Mg^{2+} ions since site mixing often leads to broadened transition [37]. It deserves to be highlighted that doping a small amount of Mg does not reduce the transition temperature, which is different from the scenario of $(Fe_{0.95}Zn_{0.05})_2Mo_3O_8$ ($T_N =$ 53.9 K) [38,39]. In the inset of Fig. 2(a), the inverse magnetic

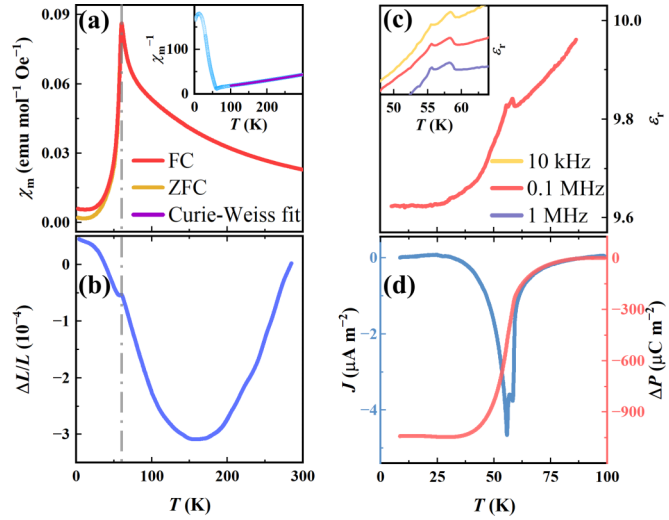

FIG. 2. Characterization of magnetization, lattice parameter, and dielectric properties. Temperature-dependent (a) molar susceptibility $\chi_m(T)$ with inset showing Curie-Weiss fitting χ_m^{-1}, (b) thermal expansion, (c) relative dielectric constant $\varepsilon_r(T)$, and (d) pyroelectric current $J(T)$ and change of electric polarization $\Delta P(T)$ along the c axis. The gray dashed line in panels (a) and (b) indicates the Néel transition. Data in the inset of panel (c) are vertically shifted for clarity. Zero point of ΔP is set at $T = 100$ K.

susceptibility above 100 K is fitted to the Curie-Weiss law:

$$\chi_m(T) = \chi_0 + \frac{C}{T+\theta}, \tag{1}$$

where χ_0 represents the temperature-independent contribution. Owing to the orbital-driven Peierls effect, the Mo^{4+} ions appear to be trimerized without contribution to the magnetism [40,41]. The effective magnetic moment ($\mu_{eff} = 4.94\,\mu_B$/Fe) is derived from the Curie constant C, which is consistent with the expected spin-only value of high-spin Fe^{2+} (4.90 μ_B).

The thermal expansion measurements clearly demonstrate that a lattice anomaly along the c axis is associated with the magnetic phase transition [Fig. 2(b)], indicating a magnetostructural correlation in FMMO. It is worth mentioning that the c parameter reaches a minimum value at a temperature far above T_N ($T_{min} = 160$ K). In the previously reported result of $Fe_2Mo_3O_8$ [36], the neutron diffraction data show a broad diffuse feature below T_{min}. The diffuse scattering, which contains information about the deviation from the average structure, is regarded as arising from the temporary or permanent breakdown of space group symmetry [42]. In FMMO, some kinds of short-range orders may be linked to the negative thermal expansion occurs below T_{min}.

A closer inspection of the data around the Néel transition indicates two clear dielectric anomalies at T_N, which are evident in $\varepsilon_r(T)$ at several frequencies [Fig. 2(c)]. The result indicates that two different dielectric characteristics are associated with the change of magnetic state. This unusual feature is consistent with the result of the temperature-dependent pyroelectric current $J(T)$ [Fig. 2(d)]. The change of polarization $\Delta P(T)$ obtained from the time integration of $J(T)$ is also shown in Fig. 2(d). A steep drop in P at T_N suggests that the long-range magnetic order causes extra polarization. It should

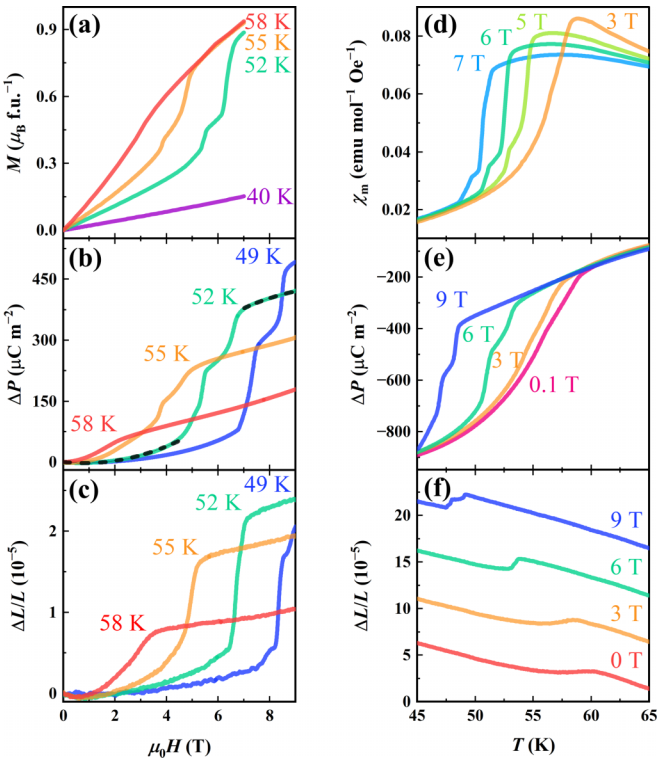

FIG. 3. Anomalies in magnetization, polarization, and lattice parameter at the magnetic phase boundaries. Magnetic-field-dependent (a) magnetization $M(H)$, (b) change of electric polarization $\Delta P(H)$, with two dashed curves showing fit to P-H curves for different magnetic states at 52 K, and (c) magnetostriction at various temperatures with magnetic field increasing along the c axis. Temperature-dependent (d) molar susceptibility $\chi_m(T)$, (e) change of electric polarization $\Delta P(T)$, and (f) thermal expansion at various magnetic fields applied along the c axis. Measurements in panels (a)–(f) are carried out along the c axis of FMMO. Zero points of ΔP are set at (b) $\mu_0 H = 0$ T and (e) $T = 100$ K, respectively. Data in panel (f) are vertically shifted for clarity.

be pointed out that no electric poling is needed to induce $\Delta P(T)$, and the polarization does not reverse its sign with a positive or negative E_{pol} (Fig. S3), indicating the pyroelectricity at T_N.

In order to reveal the potential magnetic states generated by the diluted magnetic state competition, we measure the isothermal magnetization $M(H)$ of FMMO along the c axis with magnetic field increasing [Fig. 3(a)]. The $M(H)$ curves show two evident stepwise characteristics indicating the metamagnetic transitions. In the parent compound $Fe_2Mo_3O_8$, AFM and FIM phases are controlled by the magnetic field [38] due to the frustrating sublattice couplings [35]. This competition becomes more complex in FMMO, producing two intermediate metastable magnetic states between the AFM phase and the FIM phase, which will be further discussed below.

Next, we turn to the main issue and discuss the ME effect in FMMO. Figure 3(b) demonstrates that P along the c axis is controlled by external magnetic fields. Several features of the $\Delta P(H)$ curves deserve highlighting. The ΔP increases with increasing temperature (transition from AFM to PM) or magnetic field (transition from AFM to FIM). Nevertheless, the latter shows a smaller absolute value. An identical conclusion is obtained in the study of lattice parameters (see below). Reviewing Fig. 3(b) in more detail, we find two entirely different ME responses. The field-induced ΔP increases suddenly at the transition of magnetic states but steadily in AFM and FIM states. In order to quantitatively analyze the ME effect, the ME coefficients are evaluated from the $\Delta P(H)$ curves, which can be extended to the second order as follows:

$$\Delta P = P_0 + \alpha H + \beta H^2, \tag{2}$$

where P_0 is the crystallographic and spin-induced spontaneous polarization, and α and β are the first-order and second-order ME coefficient, respectively [18]. We exemplify two fits at 52 K as indicated by the black dashed curves in Fig. 3(b). For the AFM state ($H < 4.5$ T), we obtain the first-order ME coefficient $\alpha = -8.74$ ps/m and the second-order ME coefficient $\beta = 6.51 \times 10^{-18}$ s/A. For the FIM state ($H > 7$ T), we obtain $\alpha = 104$ ps/m and $\beta = -6.12 \times 10^{-18}$ s/A. The linear ME coefficient is much larger than the counterparts of other $M_2Mo_3O_8$ members [18,20,21,38], including $Fe_2Mo_3O_8$ (-16 ps/m), $Co_2Mo_3O_8$ (28 ps/m), $Mn_2Mo_3O_8$ (-40 ps/m), and $Ni_2Mo_3O_8$ (-70 ps/m). In addition, the second-order ME coefficient exhibits significant improvement (more than ten orders of magnitude larger) compared with the parent phase (1.81×10^{-28} s/A).

To unveil the mechanism of ME effect in FMMO, we investigate the H-dependent magnetostriction ($\Delta L/L$) at various temperatures [Fig. 3(c)]. The lattice also responds sensitively to the magnetic field at the transitions of magnetic states. When the FMMO turns into the FIM state, the c axis $\Delta L/L$ shows a sharp jump, shifting toward a lower magnetic field as the temperature increases. Apparently, there is a strong spin-lattice coupling in FMMO, as expected for a polar magnet.

The relationship among magnetic states, polarization, and magnetostriction is reconfirmed under several magnetic fields as shown in Figs. 3(d)–3(f). The stepwise features in each figure accord with the experimental results mentioned above.

C. *H*-*T* phase diagram

Combining the experimental results of ε_r [Figs. S4(a) and S4(b)] and previously reported results of $Fe_2Mo_3O_8$, we construct an H-T phase diagram for FMMO in a magnetic field along the c axis as shown in Fig. 4(a). There are four ordered magnetic phases below T_N, i.e., AFM, FIM, and two metamagnetic phases (M1 and M2), distinguished by the peak-center position of ε_r. The phase boundaries are consistent with the positions of the stepwise characteristic determined by the H scan and T scan of M, P, and L [Figs. 4(a) and S5]. This feature further confirms the correctness of the phase diagram and indicates a strong correlation among magnetism, electricity, and lattice in FMMO. The forming of two additional metastable magnetic phases shown in Fig. 4(a) may be related to the multiple magnetic sites with different neighboring environments. Indeed, similar intermediate magnetic states between the AFM phase and the FIM phase are also observed in $Fe_2Mo_3O_8$ doped with Mn [18] or Zn [39]. The neutron scattering measurements under a magnetic field and theoretical calculations are urgently needed to unveil the spin

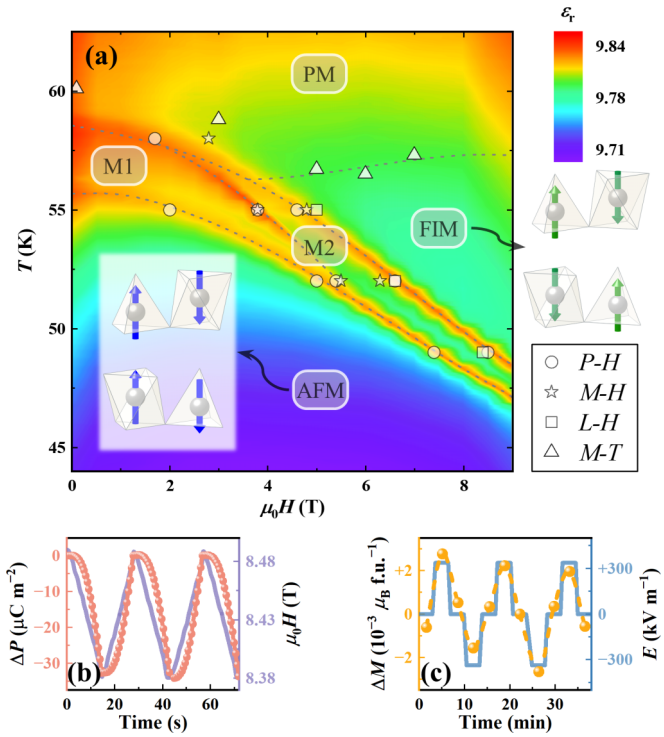

FIG. 4. H-T phase diagram and ME properties of FMMO. (a) Phase diagram is determined by variations in relative dielectric constant ε_r (color scale at upper right). Peak-center position of ε_r maps boundaries between paramagnetic phase (PM), antiferromagnetic phase (AFM), ferrimagnetic phase (FIM), and metastable magnetic phases (M1 and M2). Dashed curves in panel (a) guide the eyes to mark the phase boundaries. Spin configurations of AFM phase and FIM phase are also shown in this figure. Empty circles, empty asterisks, and empty squares indicate positions of stepwise characteristic in $P(H)$, $M(H)$, $L(H)$, and $M(T)$, respectively. (b) Modulated electric polarization (red color) as a function of time with magnetic field (purple color) varying between 8.38 and 8.49 T along the c axis at 49 K. (c) Modulated magnetization (yellow color) along the c axis at periodically electric field (blue color) varying between ± 336 kV m^{-1} with time at 52 K and $\mu_0 H = 6.3$ T. Electric field is applied along the c axis. Each point of magnetization is the average value of repeated measurements for better accuracy. The dashed curve in panel (c) guides the eyes to mark periodic oscillation of magnetization.

configurations of these two metamagnetic phases. Although a detailed investigation of the exact magnetic structures in M1 and M2 is beyond the scope of this work, this does not prevent us from exploring the ME property of FMMO.

The sharp field-induced transition at the phase boundary makes it possible to switch the polarization (magnetization) with external magnetic (electric) fields. Figure 4(b) depicts the repeated variation of P generated by a modulated magnetic field. Furthermore, the inverse effect, in which an applied electric field changes the magnetization, is also reproducible as shown in Fig. 4(c). Likewise, remarkable ME effect and inverse ME effect are also observed at other positions of the phase boundary. The sharp field-induced transitions give rise to tremendous values of the differential ME coefficient dP/dH [Fig. 5(a)], reaching 10^3 ps/m at $T = 49$ K. Different from the properties of phase boundary, the field-induced ΔP

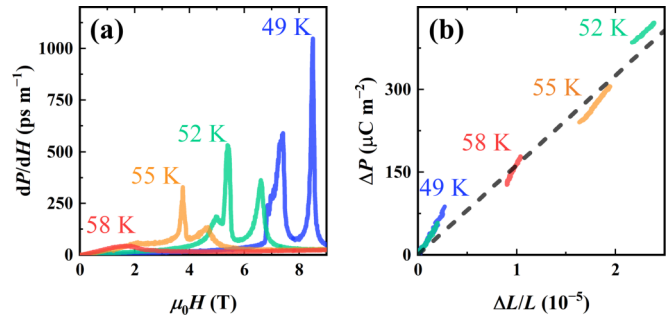

FIG. 5. ME coefficient and spin-lattice coupling of FMMO. (a) ME coefficient dP/dH estimated from the magnetic field derivative of $\Delta P(H)$ at various temperatures. (b) Variation of polarization with magnetostriction in AFM state and FIM state. Data are measured along the c axis at various temperatures. The dashed line guides the eyes to reveal linear correlation between polarization and magnetostriction.

increases steadily in AFM and FIM states, which is similar to the behavior of $\Delta L/L$. To verify the quantitative correlation between polarization and magnetostriction, which are simultaneously induced by the magnetic field, we plot the ΔP as a function of $\Delta L/L$ [Fig. 5(b)]. The nearly linear relationship will be further discussed below.

IV. DISCUSSION

As mentioned above, there are two types of ME responses in FMMO, i.e., the steady increase of ΔP in the stable magnetic phases (AFM and FIM states) and the jump of ΔP at the phase boundary. We first discuss the former case, which shows great progress of FMMO. According to the phenomenological argument based on different degrees of freedom of electrons, several mechanisms [43], i.e., spin-charge coupling, spin-orbit coupling, and spin-lattice coupling should be relevant to ME response. Considering the significant magnetostriction effect in FMMO [Fig. 3(c)], the last one is the most likely scenario. Specifically, the magnetostriction effect induced by spin-lattice coupling establishes a link between polarization and magnetism [44,45]. The nearly linear relationship between the polarization and the variation of c parameter [Fig. 5(b)] further reinforces our confidence in correctly identifying the mechanism. Therefore, the key to understanding the ME property tuned by Mg substitution is to gain a more profound insight into magnetostriction. Based on the modern electronic structure theory, magnetostriction strongly depends on the symmetry of the environment of magnetic ions. The fractional change in length $\Delta L/L$ can be obtained by minimizing the elastic energy (E_{el}) and the magnetoelastic energy (E_{me}) concerning the strain (ε_{ij}) [46,47]:

$$\frac{\partial(E_{el} + E_{me})}{\partial \varepsilon_{ij}} = 0, \tag{3}$$

where E_{me} comes from the strain-dependent part of the magnetocrystalline anisotropy energy. The introduction of Mg^{2+} ions leads to a local disturbance of the lattice to relax the strain caused by the size mismatch [27], which naturally tilts the balance between E_{el} and E_{me}. Compared with the parent phase, such a different magnetostriction property may be the reason

for the significantly improved ME coefficient. Furthermore, the preferential occupation of Mg^{2+} ions in tetrahedral sites leads to the linear ME coupling in the AFM state. In general, the $\Delta P(H)$ of an ME material is determined by the symmetry of the crystal lattice and magnetic order [1]. The magnetic point group for the AFM state of the parent phase ($6'mm'$) allows only the second-order ME effect [38], because the linear part is completely canceled by adding up the contributions of Fe^{2+} ions in different positions [48]. As for FMMO, the linear relation part of $\Delta P(H)$ data becomes reasonable, considering that Mg^{2+} ions substitute part of Fe^{2+} ions in the tetrahedral sites.

Next, we focus on the origin of the jump of ΔP. Apart from the magnetostriction, it is essential to consider the spin reorientation at the phase boundary. As reported in other spin-driven ME materials [2,16,49], P changes suddenly when a magnetic phase transition occurs. In the previous studies, the exchange-striction mechanism is employed to understand such ME coupling in $Fe_2Mo_3O_8$ [19,38,50]. The Heisenberg-like exchange striction describes an acentric displacement of charges derived from the optimizing symmetric spin product [51,52], which can be expressed as

$$\Delta P = \sum_{i,j} a_{ij} \boldsymbol{S}_i \cdot \boldsymbol{S}_j, \tag{4}$$

where a_{ij} are the exchange-striction parameters. The coefficients a_{ij} strongly depend on the bond angles and bond lengths of neighboring ions [53], which are different in AFM phase and FIM phase [19], resulting in a huge change of ΔP. The situation becomes more complicated in FMMO, as shown in Fig. 5(a). The substitution of nonmagnetic ions affects the nearest and next-nearest neighbor exchange interactions of Fe^{2+} ions [50], resulting in metamagnetic phases. Similarly, the ΔP changes when FMMO enters into the M1 or M2 state. In other words, the shifts of charged ions in response to the spin reorientations cause the ME coupling at the phase boundary.

V. CONCLUSIONS

To summarize, we have successfully doped $Fe_2Mo_3O_8$ with Mg and systematically studied the strong ME coupling of its single-crystal samples. In the H-T phase diagram of FMMO, two novel intermediate magnetic states created by introducing Mg into the oxygen tetrahedral sites compete and are balanced by magnetic field and temperature. Such an appropriate chemical doping significantly improves the ME coefficient of $Fe_2Mo_3O_8$. Six times linear ME coefficient and more than ten orders of magnitude second-order ME coefficient are achieved in FMMO. Furthermore, a giant magnetic bias is no longer necessary for the linear ME coefficient due to the change of magnetostriction property. Compared with $(Fe_{0.95}Zn_{0.05})_2Mo_3O_8$, doping a small amount of Mg does not reduce the transition temperature. These striking features discussed above contribute to the application of ME coupling, demonstrating that the FMMO is an unusual member of the $M_2Mo_3O_8$ family. In a word, the FMMO is a prototypical example where the polar structure coupled to the magnetically ordered state gives rise to a large ME coupling and further polarization. The highly consistent magnetism, polarization, and magnetostriction anomalies suggest that the spin-lattice coupling generates such a giant ME effect in FMMO. These findings of the single-phase material may open a new path for accomplishing practical ME devices with high tunability and good performance.

ACKNOWLEDGMENTS

This work was supported by the National Key Research Program of China (Grants No. 2022YFA1402801, No. 2018YFA0208402, and No. 2021YFA1400300), the National Natural Science Foundation of China (Grants No. 11874413, No. 11934017, and No. 51972333), and the Strategic Priority Research Program of the Chinese Academy of Sciences (CAS) (Grant No. XDB33000000). X.S. was sponsored by the Youth Innovation Promotion Association of CAS (Grant No. 2019009).

R.Y. conceived and supervised the project. J.Y., D.S., and J.H. carried out the research and analyzed dielectric property and magnetostriction data. Y.J., Q.G., Y.M., X.L., and L.W. helped to prepare the samples for measurements. X.S. conducted the STEM measurement. J.Y., Y.Y., Y.L., Y.S., and R.Y. analyzed data. J.Y., X.S., and R.Y. wrote the manuscript, and all authors amended the manuscript.

[1] M. Fiebig, Revival of the magnetoelectric effect, J. Phys. D: Appl. Phys. **38**, R123 (2005).

[2] S.-W. Cheong and M. Mostovoy, Multiferroics: A magnetic twist for ferroelectricity, Nat. Mater. **6**, 13 (2007).

[3] M. Fiebig, T. Lottermoser, D. Meier, and M. Trassin, The evolution of multiferroics, Nat. Rev. Mater. **1**, 16046 (2016).

[4] J. Ma, J. Hu, Z. Li, and C.-W. Nan, Recent progress in multiferroic magnetoelectric composites: From bulk to thin films, Adv. Mater. **23**, 1062 (2011).

[5] N. A. Spaldin and R. Ramesh, Advances in magnetoelectric multiferroics, Nat. Mater. **18**, 203 (2019).

[6] W. F. Brown, R. M. Hornreich, and S. Shtrikman, Upper Bound on the Magnetoelectric Susceptibility, Phys. Rev. **168**, 574 (1968).

[7] Y. F. Popov, A. K. Zvezdin, G. P. Vorob'ev, A. M. Kadomtseva, V. A. Murashev, and D. N. Rakov, Linear magnetoelectric effect and phase transitions in bismuth ferrite, $BiFeO_3$, JETP Lett. **57**, 69 (1993).

[8] C. Lu, M. Wu, L. Lin, and J.-M. Liu, Single-phase multiferroics: New materials, phenomena, and physics, Natl. Sci. Rev. **6**, 653 (2019).

[9] J. T. Heron, J. L. Bosse, Q. He, Y. Gao, M. Trassin, L. Ye, J. D. Clarkson, C. Wang, J. Liu, S. Salahuddin *et al.*, Deterministic switching of ferromagnetism at room temperature using an electric field, Nature (London) **516**, 370 (2014).

[10] T. Kimura, T. Goto, H. Shintani, K. Ishizaka, T. Arima, and Y. Tokura, Magnetic control of ferroelectric polarization, Nature (London) **426**, 55 (2003).

[11] N. Hur, S. Park, P. A. Sharma, J. S. Ahn, S. Guha, and S.-W. Cheong, Electric polarization reversal and memory in a multiferroic material induced by magnetic fields, Nature (London) **429**, 392 (2004).

[12] Y. J. Jo, S. Lee, E. S. Choi, H. T. Yi, W. Ratcliff, Y. J. Choi, V. Kiryukhin, S. W. Cheong, and L. Balicas, 3:1 magnetization plateau and suppression of ferroelectric polarization in an Ising chain multiferroic, Phys. Rev. B **79**, 012407 (2009).

[13] T. Kimura, J. C. Lashley, and A. P. Ramirez, Inversion-symmetry breaking in the noncollinear magnetic phase of the triangular-lattice antiferromagnet $CuFeO_2$, Phys. Rev. B **73**, 220401(R) (2006).

[14] L. D. Landau, E. M. Lifshitz, and L. P. Pitaevskii, *Electrodynamics of Continuous Media*, 2nd ed., rev. and enl. (Pergamon, Oxford, 1984).

[15] S.-W. Cheong, D. Talbayev, V. Kiryukhin, and A. Saxena, Broken symmetries, non-reciprocity, and multiferroicity, npj Quantum Mater. **3**, 19 (2018).

[16] Y. S. Oh, S. Artyukhin, J. J. Yang, V. Zapf, J. W. Kim, D. Vanderbilt, and S.-W. Cheong, Non-hysteretic colossal magnetoelectricity in a collinear antiferromagnet, Nat. Commun. **5**, 3201 (2014).

[17] Y.-S. Chai, J.-Z. Cong, J.-C. He, D. Su, X.-X. Ding, J. Singleton, V. Zapf, and Y. Sun, Giant magnetostriction and non-saturating electric polarization up to 60 T in the polar magnet $CaBaCo_4O_7$, Phys. Rev. B **103**, 174433 (2021).

[18] T. Kurumaji, S. Ishiwata, and Y. Tokura, Diagonal magnetoelectric susceptibility and effect of Fe doping in the polar ferrimagnet $Mn_2Mo_3O_8$, Phys. Rev. B **95**, 045142 (2017).

[19] Y. Wang, G. L. Pascut, B. Gao, T. A. Tyson, K. Haule, V. Kiryukhin, and S.-W. Cheong, Unveiling hidden ferrimagnetism and giant magnetoelectricity in polar magnet $Fe_2Mo_3O_8$, Sci. Rep. **5**, 12268 (2015).

[20] Y. S. Tang, G. Z. Zhou, L. Lin, R. Chen, J. F. Wang, C. L. Lu, L. Huang, J. H. Zhang, Z. B. Yan, X. M. Lu *et al.*, Successive electric polarization transitions induced by high magnetic field in the single-crystal antiferromagnet $Co_2Mo_3O_8$, Phys. Rev. B **105**, 064108 (2022).

[21] Y. S. Tang, J. H. Zhang, L. Lin, R. Chen, J. F. Wang, S. H. Zheng, C. Li, Y. Y. Zhang, G. Z. Zhou, L. Huang *et al.*, Metamagnetic transitions and magnetoelectricity in the spin-1 honeycomb antiferromagnet $Ni_2Mo_3O_8$, Phys. Rev. B **103**, 014112 (2021).

[22] W. H. McCarroll, L. Katz, and R. Ward, Some ternary oxides of tetravalent molybdenum, J. Am. Chem. Soc. **79**, 5410 (1957).

[23] S. Yu, B. Gao, J. W. Kim, S.-W. Cheong, M. K. L. Man, J. Madéo, K. M. Dani, and D. Talbayev, High-Temperature Terahertz Optical Diode Effect without Magnetic Order in Polar $FeZnMo_3O_8$, Phys. Rev. Lett. **120**, 037601 (2018).

[24] T. Ideue, T. Kurumaji, S. Ishiwata, and Y. Tokura, Giant thermal Hall effect in multiferroics, Nat. Mater. **16**, 797 (2017).

[25] S. Park, N. Nagaosa, and B.-J. Yang, Thermal Hall effect, spin Nernst effect, and spin density induced by a thermal gradient in collinear ferrimagnets from magnon–phonon interaction, Nano Lett. **20**, 2741 (2020).

[26] R. P. Chaudhury, F. Ye, J. A. Fernandez-Baca, B. Lorenz, Y. Q. Wang, Y. Y. Sun, H. A. Mook, and C. W. Chu, Robust ferroelectric state in multiferroic $Mn_{1-x}Zn_xWO_4$, Phys. Rev. B **83**, 014401 (2011).

[27] V. Cuartero, J. Blasco, J. A. Rodríguez-Velamazán, J. García, G. Subías, C. Ritter, J. Stankiewicz, and L. Canadillas-Delgado, Effects of Al substitution on the multiferroic properties of $TbMnO_3$, Phys. Rev. B **86**, 104413 (2012).

[28] Y. S. Tang, S. M. Wang, L. Lin, C. Li, S. H. Zheng, C. F. Li, J. H. Zhang, Z. B. Yan, X. P. Jiang, and J.-M. Liu, Collinear magnetic structure and multiferroicity in the polar magnet $Co_2Mo_3O_8$, Phys. Rev. B **100**, 134112 (2019).

[29] V. Caignaert, A. Maignan, K. Singh, Ch. Simon, V. Pralong, B. Raveau, J. F. Mitchell, H. Zheng, A. Huq, and L. C. Chapon, Gigantic magnetic-field-induced polarization and magnetoelectric coupling in a ferrimagnetic oxide $CaBaCo_4O_7$, Phys. Rev. B **88**, 174403 (2013).

[30] P. Strobel, Y. Le Page, and S. P. McAlister, Growth and physical properties of single crystals of $Fe_2^{II}Mo_3^{IV}O_8$, J. Solid State Chem. **42**, 242 (1982).

[31] Y. Ma, Y. Wang, J. Cong, and Y. Sun, Magnetic-Field Tuning of Hydrogen Bond Order-Disorder Transition in Metal-Organic Frameworks, Phys. Rev. Lett. **122**, 255701 (2019).

[32] See Supplemental Material at http://link.aps.org/supplemental/10.1103/PhysRevB.107.104408 for the crystal structure, pyroelectricity, and details of the H-T phase diagram.

[33] R. D. Shannon, Revised effective ionic radii and systematic studies of interatomic distances in halides and chalcogenides, Acta Crystallogr., Sect. A: Found. Adv. **32**, 751 (1976).

[34] F. Varret, H. Czeskleba, F. Hartmann-Boutron, and P. Imbert, Étude par effet Mössbauer de l'ion Fe^{2+} en symétrie trigonale dans les composés du type $(Fe, M)_2Mo_3O_8$ (M = Mg, Zn, Mn, Co, Ni) et propriétés magnétiques de $(Fe, Zn)_2Mo_3O_8$, J. Phys. **33**, 549 (1972).

[35] D. Bertrand and H. Kerner-Czeskleba, Étude structurale et magnétique de molybdates d'éléments de transition, J. Phys. **36**, 379 (1975).

[36] S. Reschke, A. A. Tsirlin, N. Khan, L. Prodan, V. Tsurkan, I. Kézsmárki, and J. Deisenhofer, Structure, phonons, and orbital degrees of freedom in $Fe_2Mo_3O_8$, Phys. Rev. B **102**, 094307 (2020).

[37] J. R. Morey, A. Scheie, J. P. Sheckelton, C. M. Brown, and T. M. McQueen, $Ni_2Mo_3O_8$: Complex antiferromagnetic order on a honeycomb lattice, Phys. Rev. Mater. **3**, 014410 (2019).

[38] T. Kurumaji, S. Ishiwata, and Y. Tokura, Doping-Tunable Ferrimagnetic Phase with Large Linear Magnetoelectric Effect in a Polar Magnet $Fe_2Mo_3O_8$, Phys. Rev. X **5**, 031034 (2015).

[39] W. Wang, P. Z. Li, Y. T. Chang, M. F. Liu, C. L. Lu, X. B. Lu, M. Zeng, and J.-M. Liu, Effect of nonmagnetic substituent Zn on the phase competition and multiferroic properties in the polar magnet $Fe_2Mo_3O_8$, Appl. Phys. Lett. **118**, 112901 (2021).

[40] D. I. Khomskii and S. V. Streltsov, Orbital effects in solids: Basics, recent progress, and opportunities, Chem. Rev. **121**, 2992 (2021).

[41] D. I. Khomskii, T. Mizokawa, and S. V. Streltsov, Comment on "Spin-Lattice Coupling and the Emergence of the Trimerized Phase in the $S = 1$ Kagome Antiferromagnet $Na_2Ti_3Cl_8$," Phys. Rev. Lett. **127**, 049701 (2021).

[42] V. M. Nield and D. A. Keen, *Diffuse Neutron Scattering from Crystalline Materials* (Clarendon, New York, 2001).

[43] S. Dong, H. Xiang, and E. Dagotto, Magnetoelectricity in multiferroics: A theoretical perspective, Natl. Sci. Rev. **6**, 629 (2019).

[44] R. P. Chaudhury, B. Lorenz, Y. Y. Sun, L. N. Bezmaternykh, V. L. Temerov, and C. W. Chu, Magnetoelectricity and

magnetostriction due to the rare-earth moment in $TmAl_3(BO_3)_4$, Phys. Rev. B **81**, 220402(R) (2010).

[45] K.-C. Liang, R. P. Chaudhury, B. Lorenz, Y. Y. Sun, L. N. Bezmaternykh, V. L. Temerov, and C. W. Chu, Giant magnetoelectric effect in $HoAl_3(BO_3)_4$, Phys. Rev. B **83**, 180417(R) (2011).

[46] A. E. Clark, Magnetostrictive rare earth-Fe_2 compounds, *Handbook of Ferromagnetic Materials* (Elsevier, New York, 1980), Vol. 1, pp. 531–589.

[47] P. Nieves, S. Arapan, S. H. Zhang, A. P. Kądzielawa, R. F. Zhang, and D. Legut, MAELAS: MAgneto-ELAStic properties calculation via computational high-throughput approach, Comput. Phys. Commun. **264**, 107964 (2021).

[48] M. Eremin, K. Vasin, and A. Nurmukhametov, On the theory of magnetoelectric coupling in $Fe_2Mo_3O_8$, Materials **15**, 8229 (2022).

[49] K. Yoo, B. Koteswararao, J. Kang, A. Shahee, W. Nam, F. F. Balakirev, V. S. Zapf, N. Harrison, A. Guda, N. Ter-Oganessian *et al.*, Magnetic field-induced ferroelectricity in $S = 1/2$ kagome staircase compound $PbCu_3TeO_7$, npj Quantum Mater. **3**, 45 (2018).

[50] I. V. Solovyev and S. V. Streltsov, Microscopic toy model for magnetoelectric effect in polar $Fe_2Mo_3O_8$, Phys. Rev. Mater. **3**, 114402 (2019).

[51] I. A. Sergienko and E. Dagotto, Role of the Dzyaloshinskii-Moriya interaction in multiferroic perovskites, Phys. Rev. B **73**, 094434 (2006).

[52] I. A. Sergienko, C. Şen, and E. Dagotto, Ferroelectricity in the Magnetic E-Phase of Orthorhombic Perovskites, Phys. Rev. Lett. **97**, 227204 (2006).

[53] M. Mochizuki, N. Furukawa, and N. Nagaosa, Spin Model of Magnetostrictions in Multiferroic Mn Perovskites, Phys. Rev. Lett. **105**, 037205 (2010).